

4D Collaborative Non-Local Means Based Diffusion MRI Denoising

Geng Chen, Yafeng Wu*

Data Processing Center, Northwestern Polytechnical University, Xi'an, China

ABSTRACT: Noise is a major issue that reduces the quality of images acquired by diffusion MRI (dMRI). Recently, the non-local means (NLM) algorithm has been proposed and successfully applied in dMRI denoising. However, NLM relies on self-similarity information and tends to fail when recurrent image structures cannot be located. To address this issue, we introduce the improved collaborative NLM. Both inner-image and inter-image similarity information are used. Specifically, a group of co-denoising images are first registered to the target space. NLM-like block matching is then performed on both target noisy image and co-denoising images. This formulation can significantly increase the amount of similarity information and reduce the rare patch effect. Moreover, in order to adapt to the characteristics of dMRI, we present a complete denoising framework with multiple techniques including 4D image block, pseudo-residual-based noise standard deviation estimation, Rician bias correction, and block preselection. Extensive experiments on both synthetic and real data demonstrate that the proposed framework outperforms the classical NLM method.

Keywords: Block Matching, Denoising, Diffusion MRI, Non-Local Means, Kernel Regression.

I. INTRODUCTION

Diffusion magnetic resonance imaging (dMRI) [1] is capable of measuring the diffusion process of water molecules in human brain non-invasively. Based on the diffusion properties obtained, tractography can then reconstruct white matter tracts [2,3]. Therefore, white matter integrity and degeneration can be effectively examined and brain connectome [4] can be further revealed among the development of nervous system [5] and a variety of neurological diseases such as Alzheimer's disease [6-10], autism [11,12], brain traumatic injury [13,14], and even genetics [15,16]. Since dMRI measures the signal attenuation caused by water diffusion, the images acquired tend to have low signal-to-noise ratio (SNR). Moreover, dMRI requires acquiring a large amount of images, which is very time consuming. To save the acquisition time, fast imaging protocol becomes necessary; however, it further decreases the SNR. The images with low SNR create significant difficulty for the following image analyses and may result in unreliable conclusions. Therefore, denoising plays an important role in the preprocessing of dMRI images.

Recently, the non-local means (NLM) [17] algorithm has been applied in dMRI studies and shown promising performance in denoising [18], super resolution [19] and voxel-based morphometry [20]. NLM estimates the true signals from the self-similarity information of image collected by block matching. However, the denoising performance is largely affected by the amount of self-similarity information. NLM fails when the matching features of certain unique structures cannot be located, which causes so-called "rare patch effect" [21]. To resolve this problem, Prime et al. [22] extended the NLM search volume to the symmetrical parts of human brain in order to increase the chance of locating matching structures. Although it improved the denoising performance, only doubling the search volume may not be sufficient. Chen et al. [23,24] introduced the inter-image similarity information by utilizing other co-denoising images. This formulation, named collaborative NLM (CNLM), significantly increases the amount of similarity information and thus reduces the influence of "rare patch effect" effectively. However, CNLM is designed only for structural MRI denoising, which may not be suitable based on the characteristics of dMRI.

To apply CNLM in dMRI, a major algorithm extension is to re-define the image blocks used in block matching. Diffusion images can be considered as vector-based or 4D images while all the volumes are stacked together. Hence, the 3D image block used in the original CNLM cannot be directly applied in dMRI. Yap et al. [18] constructed 4D image blocks from 3D image blocks extracted from a set of diffusion images and those 4D image blocks were then applied in block matching. It has been demonstrated that 4D image block is able to obtain more robust block matching performance than 3D image block. Another benefit for this formulation is high efficiency. When using 3D image blocks, we need to compute NLM weights in each individual image.

Therefore, the computation has to be performed multiple times to process the entire diffusion dataset. In contrast, 4D image block allows NLM weights to be computed only one time and diffusion images can be denoised jointly.

In this paper, we propose a complete framework in dMRI denoising with 4D CNLM, in which both inner and inter-image similarity information are used. 4D image blocks are applied to adapt the 4D characteristic of dMRI. Pseudo-residual [25] is used to get robust estimation of noise variance used in the calculation of NLM weights. Moreover, we utilize Rician bias correction [26] to adapt to the characteristics of dMRI noise and block preselection [25] to save the computational time. The proposed framework will be validated on both synthetic data and real human data to demonstrate its performance.

II. METHOD

2.1. Non-local means

Our method is based on the NLM algorithm. We first provide a quick review on the classical NLM algorithm. NLM has two major components, i.e., weighted average and block matching. Given a location \mathbf{x}_i , the first component takes the weighted average of all intensity values in the search volume to obtain the NLM recovered value $NL(u)(\mathbf{x}_i)$, i.e.,

$$NL(u)(\mathbf{x}_i) = \sum_{\mathbf{x}_j \in \mathcal{V}(\mathbf{x}_i)} w(\mathbf{x}_i, \mathbf{x}_j) u(\mathbf{x}_j), \tag{1}$$

where $\mathcal{V}(\mathbf{x}_i)$ is a cubic search volume centered at \mathbf{x}_i , and the size of $\mathcal{V}(\mathbf{x}_i)$ is $3(d + 1)$. $u(\mathbf{x}_j)$ is the intensity value at \mathbf{x}_j . The second component compares two blocks and assigns a weight to indicate the similarity between two blocks. Let \mathcal{N}_i be a cubic neighbor centered at \mathbf{x}_i , and the size of \mathcal{N}_i is $3(m + 1)$. We then define $u(\mathcal{N}_i)$ to be a vector containing all intensity values in \mathcal{N}_i . The weight $w(\mathbf{x}_i, \mathbf{x}_j)$ between \mathbf{x}_i and \mathbf{x}_j is then defined as a Gaussian function of the Euclidean distance between $u(\mathcal{N}_i)$ and $u(\mathcal{N}_j)$, i.e.,

$$w(\mathbf{x}_i, \mathbf{x}_j) = \frac{1}{Z_i} \exp \left\{ -\frac{\|u(\mathcal{N}_i) - u(\mathcal{N}_j)\|_2^2}{h_i^2} \right\}, \tag{2}$$

where h_i controls the attenuation of exponential equation; Z_i is a constant that guarantees that the sum of the weights equals one, i.e., $\sum_{\mathbf{x}_j \in \mathcal{V}(\mathbf{x}_i)} w(\mathbf{x}_i, \mathbf{x}_j) = 1$. The definition of Z_i then becomes

$$Z_i = \sum_{\mathbf{x}_j \in \mathcal{V}(\mathbf{x}_i)} \exp \left\{ -\frac{\|u(\mathcal{N}_i) - u(\mathcal{N}_j)\|_2^2}{h_i^2} \right\}. \tag{3}$$

We observe that $0 \leq w(\mathbf{x}_i, \mathbf{x}_j) \leq 1$. When \mathbf{x}_i and \mathbf{x}_j are the same, the weight will become one, which is too large in practice. Hence, we set $w(\mathbf{x}_i, \mathbf{x}_i) = \max(w(\mathbf{x}_i, \mathbf{x}_j)), \forall i \neq j$.

2.2. 4D Collaborative Non-local Means

4D CNLM introduces multiple co-denoising images to help denoise the target image. Specifically, co-denoising images are first warped to the target space. Then, block matching is not only performed in the search volume of the target image but also in those of co-denoising images. Hence, both inner-image and inter-image similarities can be captured in the weighted average and the performance is thus greatly improved. An overview of 4D CNLM is shown in Fig. 1.

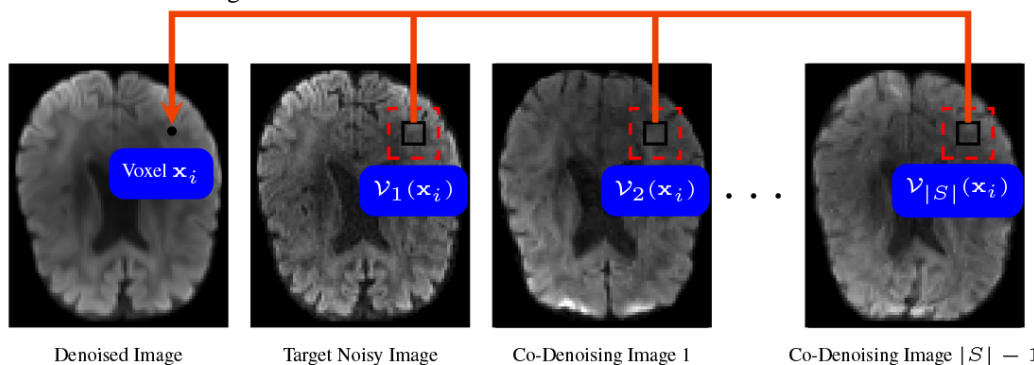


Fig. 1: An overview of 4D CNLM. The intensity value of the denoised target image voxel is decided based on those of the voxels in a set of search volumes located in both the target noisy image and the co-denoising images. Note that here all the diffusion image voxels are vector-valued or 4D.

Suppose we have an image group \mathcal{G} , including one target noisy image and $|\mathcal{G}| - 1$ co-denosing images. The recovered diffusion signals given by 4D CNLM is:

$$NL(\mathbf{u})(\mathbf{x}_i) = \frac{\sum_{k \in \mathcal{G}} \sum_{\mathbf{x}_j \in \mathcal{V}_k(\mathbf{x}_i)} \hat{w}_k(\mathbf{x}_i, \mathbf{x}_j) \mathbf{u}(\mathbf{x}_j)}{\sum_{k \in \mathcal{G}} \sum_{\mathbf{x}_j \in \mathcal{V}_k(\mathbf{x}_i)} \hat{w}_k(\mathbf{x}_i, \mathbf{x}_j)}, \tag{4}$$

where $\mathcal{V}_k(\mathbf{x}_i)$ is a search volume centered at \mathbf{x}_i in image $k \in \mathcal{G}$. $\hat{w}_k(\mathbf{x}_i, \mathbf{x}_j)$ is an un-normalized weight between \mathbf{x}_i and \mathbf{x}_j . $\mathbf{u}(\mathbf{x}_j)$ is a vector containing all diffusion voxels in \mathbf{x}_j . Due to the 4D property of dMRI, instead of the 3D block defined in Eq.(2), we defined a 4D block \mathcal{B}_i consisting of a group of 3D blocks, i.e., $\mathcal{B}_i = \{\mathcal{N}_l(\mathbf{q}_l) | l = 1, \dots, L\}$. Each 3D block $\mathcal{N}_l(\mathbf{q}_l)$ represents a cubic neighborhood centered at \mathbf{x}_i in the diffusion image acquired using gradient direction \mathbf{q}_l . The weight between two 4D blocks is then defined as

$$\hat{w}_k(\mathbf{x}_i, \mathbf{x}_j) = \exp \left\{ -\frac{1}{L} \sum_{l=1}^L \frac{\| \mathbf{u}(\mathcal{N}_l(\mathbf{q}_l)) - \mathbf{u}(\mathcal{N}_l(\mathbf{q}_l)) \|_2^2}{h_l^2(\mathbf{q}_l)} \right\}, \tag{5}$$

NLM can then be regarded as a non-parametric kernel regression problem. Chen et al. [23,24] showed that increasing the sample size alone cannot reduce the estimation bias, and the corresponding bandwidth should be decreased accordingly. Hence, we define

$$h_l(\mathbf{q}_l) = \sqrt{2\beta (\hat{\sigma}_i(\mathbf{q}_l) |S|^{-\frac{1}{3}})^2 |\mathcal{N}_l(\mathbf{q}_l)|}, \tag{6}$$

where β is a constant, and $\hat{\sigma}_i(\mathbf{q}_l)$ is the estimated noise standard deviation.

2.3. Noise Standard Deviation Estimation

The parameter $h_l(\mathbf{q}_l)$ controls the attenuation of exponential function. Based on Eq. (5), $h_l(\mathbf{q}_l)$ is further determined by the estimated local noise standard deviation $\hat{\sigma}_i(\mathbf{q}_l)$. The overestimated $\hat{\sigma}_i(\mathbf{q}_l)$ brings strong smoothness in denoising, while the underestimated $\hat{\sigma}_i(\mathbf{q}_l)$ causes incomplete denoising. Hence, an accurate estimation of $\hat{\sigma}_i(\mathbf{q}_l)$ is the key to the successful denoising. We estimate $\hat{\sigma}_i(\mathbf{q}_l)$ using the robust pseudo-residual-based noise standard deviation estimation proposed in [25]. By leaving out \mathbf{q}_l for the purpose of simplification (i.e., restricting the noise estimation in one single diffusion image), we first define pseudo-residual $\epsilon(\mathbf{x}_j)$ as

$$\epsilon(\mathbf{x}_j) = \sqrt{\frac{6}{7} \left(u(\mathbf{x}_j) - \frac{1}{6} \sum_{\mathbf{x}_m \in \mathcal{P}(\mathbf{x}_j)} u(\mathbf{x}_m) \right)}, \tag{7}$$

where $\mathcal{P}(\mathbf{x}_j)$ is the six-neighbor of \mathbf{x}_j . $\hat{\sigma}_i$ is then estimated using

$$\hat{\sigma}_i = \sqrt{\frac{1}{|\mathcal{R}(\mathbf{x}_i)|} \sum_{\mathbf{x}_j \in \mathcal{R}(\mathbf{x}_i)} \epsilon^2(\mathbf{x}_j)}, \tag{8}$$

where $\mathcal{R}(\mathbf{x}_i)$ is a local volume centered at \mathbf{x}_i .

2.4. Adaption to Rician Noise

To apply the classical NLM in Rician noise removal, bias correction needs to be performed. The 2nd-order origin moment of Rician distribution follows

$$E(X^2) = \mu^2 + 2\sigma^2, \tag{9}$$

where μ is the true signal, and σ is a scale parameter to decide the level of Rician noise. Note that σ is not equal to the standard deviation of noise.

Based on Eq. (9), we then obtain the unbiased estimation using

$$NL(\mathbf{u})(\mathbf{x}_i, \mathbf{q}_l) = \sqrt{\frac{\sum_{k \in \mathcal{G}} \sum_{\mathbf{x}_j \in \mathcal{V}_k(\mathbf{x}_i)} \hat{w}_k(\mathbf{x}_i, \mathbf{x}_j) u^2(\mathbf{x}_j, \mathbf{q}_l)}{\sum_{k \in \mathcal{G}} \sum_{\mathbf{x}_j \in \mathcal{V}_k(\mathbf{x}_i)} \hat{w}_k(\mathbf{x}_i, \mathbf{x}_j)} - 2\hat{\sigma}}. \tag{10}$$

where $\hat{\sigma}$ is an estimate of σ and can be estimated from the image background using the method presented in [26].

2.5. Block Preselection

4D CNLM requires multiple search volumes in denoising, which causes astronomical computational burden. To make the algorithm efficient, a straightforward solution is to add a block preselection step.

Specifically, before the weight calculation, the search blocks far from the target block are discarded, and only some similar search blocks are kept. A preselection scheme based on block statistics [25] is shown below:

$$\hat{w}_k(\mathbf{x}_i, \mathbf{x}_j) = \exp \left\{ -\frac{1}{L} \sum_{l=1}^L \frac{\| \mathbf{u}(\mathcal{N}_i(\mathbf{q}_l)) - \mathbf{u}(\mathcal{N}_j(\mathbf{q}_l)) \|_2^2}{h_l^2(\mathbf{q}_l)} \right\} \quad (11)$$

only if

$$\left(\mu_1 < \frac{\overline{\mathbf{u}(\mathcal{B}_i)}}{\overline{\mathbf{u}(\mathcal{B}_j)}} < \frac{1}{\mu_1} \vee \mu_1 < \frac{\text{inv}(\overline{\mathbf{u}(\mathcal{B}_i)})}{\text{inv}(\overline{\mathbf{u}(\mathcal{B}_j)})} < \frac{1}{\mu_1} \right) \wedge \sigma_1^2 < \frac{\text{var}(\mathbf{u}(\mathcal{B}_i))}{\text{var}(\mathbf{u}(\mathcal{B}_j))} < \frac{1}{\sigma_1^2} \quad (12)$$

Otherwise, $\hat{w}_k(\mathbf{x}_i, \mathbf{x}_j) = 0$, where $\overline{\mathbf{u}(\mathcal{B}_i)}$, $\text{inv}(\overline{\mathbf{u}(\mathcal{B}_i)})$ and $\text{var}(\mathbf{u}(\mathcal{B}_i))$ are the mean, the inverted mean, and the variance of 4D block \mathcal{B}_i , respectively. The parameters $0 < \mu_1 < 1$ and $0 < \sigma_1 < 1$ are two thresholds. The inverted mean is defined as

$$\text{inv}(\overline{\mathbf{u}(\mathcal{B}_i)}) = \max(\overline{\mathbf{u}(\mathcal{B}_i)}) - \overline{\mathbf{u}(\mathcal{B}_i)}. \quad (13)$$

III. DATASETS

3.1. Synthetic Dataset

A set of synthetic spiral diffusion data was generated to evaluate the algorithm performance. Each fiber population was modeled by a tensor with $\lambda_1 = 1.7 \times 10^{-3} \text{mm}^3/\text{s}$, $\lambda_2 = \lambda_3 = 3 \times 10^{-4} \text{mm}^3/\text{s}$, and $b = 1000 \text{ s/mm}^2$. The baseline signal without diffusion attenuation was set to 150. 30 diffusion directions consistent with the real data were applied in the simulation. The image was set to 128×128 . To simulate the registration errors between images, 10 sets of rigid transformations were applied to the target ground truth image to generate the co-denoising images. The rigid transformation included random translations from -4mm to 4mm along each axis. Finally, four levels of Rician noise (3%, 6%, 9%, 12%) were added to the 11 ground truth images. The noise level $p\%$ indicated how much Gaussian noise (i.e., $\mathcal{N}(0, v * (p/100))$) was added in the complex domain of the signal, where v was the maximum signal value (150 in our case). The Rician noise was simulated using the method proposed in [25].

3.2. Real Human Dataset

The diffusion images from 11 subjects were acquired with a Siemens 3T TIM Trio MR scanner. The standard acquisition protocol is: 30 diffusion volumes with the diffusion directions uniformly distributed on a hemisphere with $b = 1000 \text{ s/mm}^2$ and one volume with no diffusion weighting, image size 128×128 , voxel size $2 \times 2 \times 2 \text{ mm}^3$, TE=81ms, TR=7618ms, and 1 average. The diffusion images of one subject were used as the target images, while the rest were used as co-denoising images. Before performing 4D CNLM, we warped the co-denoising images to the target space using a large deformation diffeomorphic registration algorithm [27,28] designed for dMRI registration.

IV. RESULTS

For all experiments, we set $d=1$, $m=2$, $\beta=1$. Note that the resolution of dMRI is low, therefore, we did not use a large radius for the image block and search volume. $|G|$ was set to 11, including one target noisy image and 10 co-denoising images. In the experiments, we compared three methods including 4D CNLM, NLM and simple averaging. The methods were also evaluated in high order entities, i.e., orientation distribution function (ODF), and we used the method proposed in [29] to reconstruct ODFs.

Peak-to-signal-ratio (PSNR) was used for the quantitatively evaluation. The definition follows

$$\text{PSNR} = 20 \log_{10} \frac{\text{MAX}}{\text{RMSE}} \quad (14)$$

where RMSE represents for root mean square error, MAX is the maximum intensity value of the input image (150 in our case).

3.1. Synthetic Data

The PSNR results of synthetic data are shown in Fig. 2. 4D CNLM gets the highest PSNR values at all noise levels. Compared to NLM, the largest improvement, 7.67 dB, happens at the noise level of 6%. The better PSNR value indicates the denoised image is closer to the ground truth. In contrast, simple averaging gives the lowest PSNR due to the simulated misalignment between images. NLM-based methods utilize robust block matching to correct inter-image misalignment and significantly improve the denoising performance. 4D CNLM utilizes a sufficient number of co-denoising images. From Fig. 3, we can observe that the PSNR value increases when more co-denoising images are used in denoising. The ODF reconstruction results, shown in Fig.4, demonstrate that 4D CNLM gives clean and coherent ODFs. Compared to other three methods, shown in (C), (D), and (F), the ODFs estimated with 4D CNLM is the closest to the ground truth.

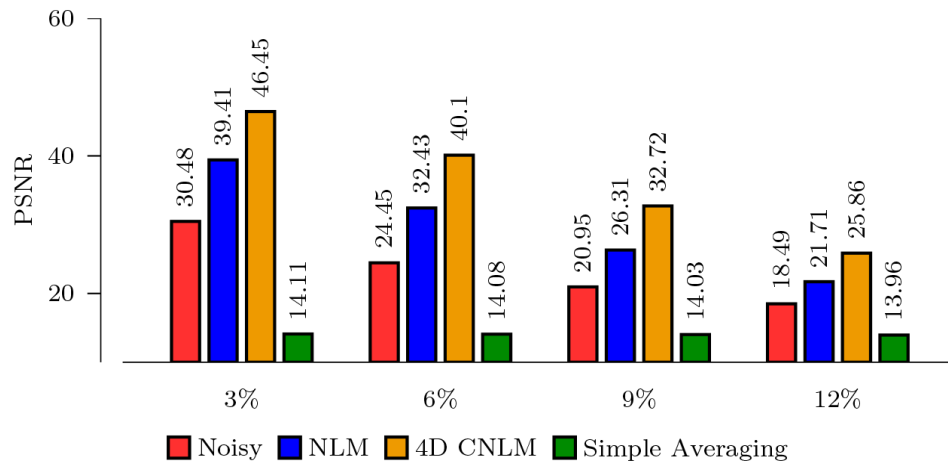


Fig. 2: PSNR comparisons between simple averaging, NLM, and 4D CNLM at different noise levels. Note that 10 co-denoising images are used in 4D CNLM and simple averaging.

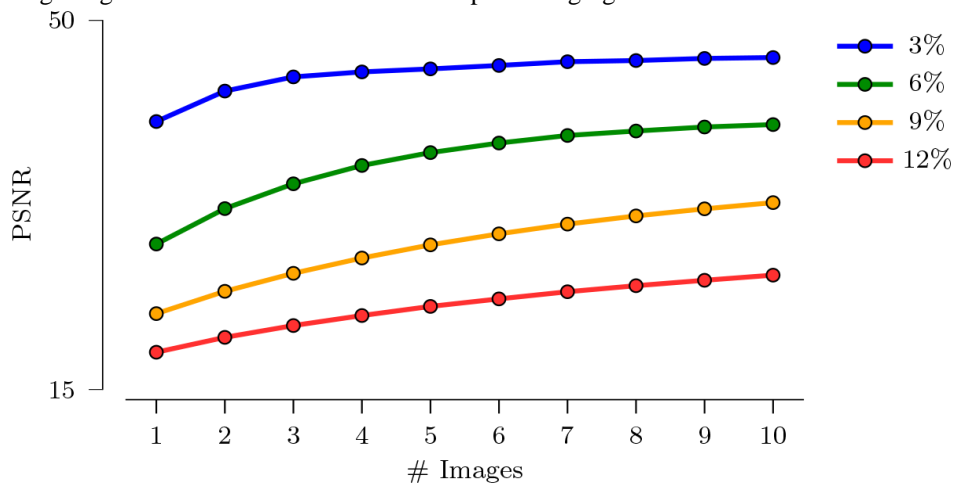


Fig. 3:The PSNR performance using different numbers of co-denoising images at different noise levels.

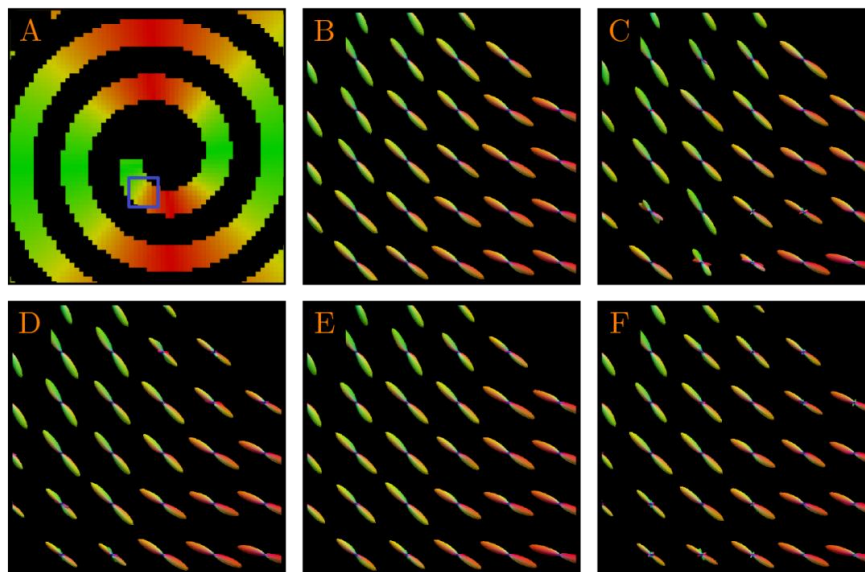


Fig. 4: Comparison of ODF visualization in synthetic data. (A) a direction-encoded color FA image for reference. The rest five images are the close-up views for the blue square in (A). (B) is the ground truth; (C) is a noisy version of (B); (D), (E) and (F) are the denoising versions using NLM, 4D CNLM and simple averaging, respectively. 10 co-denoising images are used in (E) and (F).

3.2. Real Human Data

From Fig. 5, we can observe that 4D CNLM is able to preserve important local subtle structures after denoising. The local subtle structures in grey matter area contain important information for disease diagnosis and are the basis of successful cortical surface extraction [30]. We also evaluated the influence of denoising in the ODF reconstruction. The ODF results, shown in Fig.6, indicate that 4D CNLM gives more coherent and clean ODFs. Plenty of spurious peaks can be seen in the ODFs reconstructed using the noisy data and NLM denoised data.

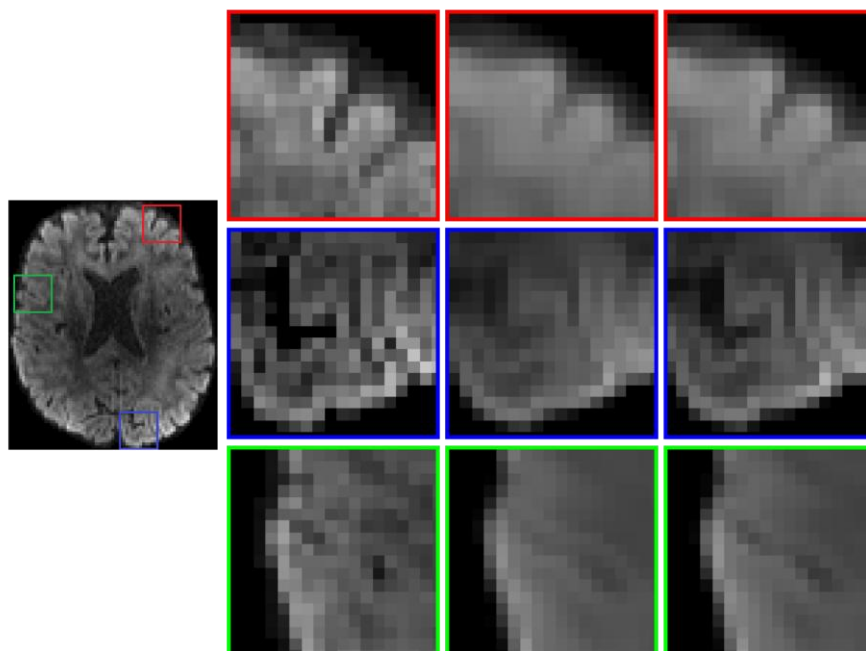


Fig. 5: Denoising of real data. (Far Left) Reference DW image. Regional close-up views for (Left) noisy DW image, (Middle) NLM denoised DW image, and (Right) 4D CNLM denoised DW image using 10 co-denoising images.

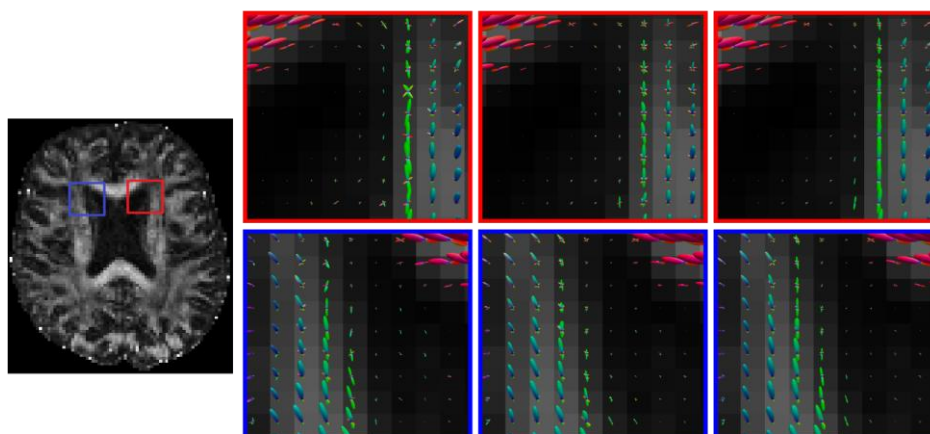


Fig 6: Comparison of ODFs in real human data. (Far Left) Reference FA image. ODFs estimated using (Left) noisy dMRI data, (Middle) NLM denoised dMRI data, and (Right) 4D CNLM dMRI data with 10 co-denoising images.

V. CONCLUSION

In this work, we propose a complete framework for dMRI denoising with 4D CNLM. 4D image block is used to adapt the characteristics of dMRI. Pseudo-residual is utilized to achieve robust noise standard deviation estimation. Ricain bias correction is considered to recover unbiased estimation. Finally, block perselection is added to reduce computational burden. Extensive experiments on synthetic data and real human data demonstrate that our method outperforms classical NLM algorithm. Further ODF results illustrate that the denoised images with our method can provide clean and coherent fiber orientations.

VI. Acknowledgements

The first author was supported by a scholarship from China Scholar Council (CSC).

REFERENCES

- [1] H. Johansen-Berg and T. E. Behrens, Eds., Diffusion MRI - from quantitative measurement to in vivo neuroanatomy, *Academic Press*, 2009.
- [2] Y. Jin and H. E. Cetinçul, Tractography-embedded white matter stream clustering, *IEEE 12th international symposium on Biomedical imaging (ISBI)*, New York, USA, 2015, 432-435.
- [3] Y. Jin, Y. Shi, L. Zhan, J. Li, G. I. de Zubicaray, K. L. McMahon, N. G. Martin, M. J. Wright, and P. M. Thompson, Automatic population HARDI white matter tract clustering by label fusion of multiple tract atlases, *Multimodal brain image analysis, LNCS 7509*, Nice, France, 2012, 147-156.
- [4] P.-T. Yap, G. Wu, and D. Shen, Human brain connectomics: Networks, techniques, and applications, *IEEE Signal Processing Magazine*, 27(4), 2010, 131-134.
- [5] P.-T. Yap, Y. Fan, Y. Chen, J. Gilmore, W. Lin, and D. Shen, Development trends of white matter connectivity in the first years of life, *PLoS ONE*, 6(9), 2011, e24678.
- [6] C.-Y. Wee, P.-T. Yap, W. Li, K. Denny, J. N. Browndyke, G. G. Potter, K. A. Welsh-Bohmer, L. Wang, and D. Shen, Enriched white matter connectivity networks for accurate identification of MCI patients, *NeuroImage*, 54(3), 2011, 1812-1822.
- [7] C.-Y. Wee, P.-T. Yap, D. Zhang, K. Denny, J. N. Browndyke, G. G. Potter, K. A. Welsh-Bohmer, L. Wang, and D. Shen, Identification of MCI individuals using structural and functional connectivity networks, *NeuroImage*, 59(3), 2012, 2045-2056.
- [8] J. Li, Y. Jin, Y. Shi, I. D. Dinov, D. J. Wang, A. W. Toga, and P. M. Thompson, Voxelwise spectral diffusional connectivity and its applications to Alzheimer's disease and intelligence prediction, *Medical image computing and computer-assisted intervention (MICCAI)*, LNCS8149, Nagoya, Japan, 2013, 655-662.
- [9] L. Zhan, J. Zhou, Y. Wang, Y. Jin, N. Jahanshad, G. Prasad, T. M. Nir, C. D. Leonardo, J. Ye, P. M. Thompson, and others, Comparison of nine tractography algorithms for detecting abnormal structural brain networks in Alzheimer's disease, *Frontiers in aging neuroscience*, 7:48, 2015. doi: 10.3389/fnagi.2015.00048.
- [10] Y. Jin, Y. Shi, L. Zhan, and P. M. Thompson, Automated multi-atlas labeling of the fornix and its integrity in Alzheimer's disease, *IEEE 12th international symposium on Biomedical imaging (ISBI)*, New York, USA, 2015, 140-143.
- [11] Y. Jin, C.-Y. Wee, F. Shi, K.-H. Thung, P.-T. Yap, D. Shen, and others, Identification of infants at risk for autism using multi-parameter hierarchical white matter connectomes, *Machine learning in medical imaging*, LNCS 9352, Munich, Germany, 2015, 170-177.
- [12] Y. Jin, C.-Y. Wee, F. Shi, K.-H. Thung, D. Ni, P.-T. Yap, and D. Shen, Identification of infants at high-risk for autism spectrum disorder using multiparameter multiscale white matter connectivity networks, *Human Brain Mapping*, 36(12), 2015, 4880-4896.
- [13] E. L. Dennis, Y. Jin, J. E. Villalon-Reina, L. Zhan, C. L. Kernan, T. Babikian, R. B. Mink, C. J. Babbitt, J. L. Johnson, C. C. Giza, P.M Thompson, and R.F Asarnow, White matter disruption in moderate/severe pediatric traumatic brain injury: Advanced tract-based analyses, *NeuroImage: Clinical*, 7, 2015, 493-505.
- [14] E. L. Dennis, M. U. Ellis, S. D. Marion, Y. Jin, L. Moran, A. Olsen, C. Kernan, T. Babikian, R. Mink, C. Babbitt, J. Johnson, C.C. Giza, P.M Thompson, and R.F Asarnow, Callosal function in pediatric traumatic brain injury linked to disrupted white matter integrity, *The Journal of Neuroscience*, 35(28), 2015, 10202-10211.
- [15] Y. Jin, Y. Shi, L. Zhan, G. I. De Zubicaray, K. L. McMahon, N. G. Martin, M. J. Wright, and P. M. Thompson, Labeling white matter tracts in HARDI by fusing multiple tract atlases with applications to genetics, *IEEE 10th international symposium on Biomedical imaging (ISBI)*, San Francisco, USA, 2013, 512-515.
- [16] Y. Jin, Y. Shi, L. Zhan, B. A. Gutman, G. I. de Zubicaray, K. L. McMahon, M. J. Wright, A. W. Toga, and P. M. Thompson, Automatic clustering of white matter fibers in brain diffusion MRI with an application to genetics, *NeuroImage*, 100, 2014, 75-90.
- [17] A. Buades, B. Coll, and J.-M. Morel, A review of image denoising algorithms, with a new one, *Multiscale Modeling & Simulation*, 4(2), 2005, 30.
- [18] P.-T. Yap, H. An, Y. Chen, and D. Shen, Uncertainty estimation in diffusion MRI using the nonlocal bootstrap, *IEEE Transactions on Medical Imaging*, 33(8), 2014, 1627-1640.
- [19] P. Coupé, J. V. Manjón, M. Chamberland, M. Descoteaux, and B. Hiba, Collaborative patch-based super-resolution for diffusion-weighted images, *NeuroImage*, 83, 2013, 245-261.
- [20] G. Chen, P. Zhang, K. Li, C.-Y. Wee, Y. Wu, D. Shen, and P.-T. Yap, Block-based statistics for robust non-parametric morphometry, *Patch-based techniques in medical imaging*, LNCS9467, Munich, Germany, 2015, 62-70.
- [21] J. Salmon and Y. Strozacki, Patch reprojections for non-local methods, *Signal Processing*, 92(2), 2012, 477-489.
- [22] S. Prima and O. Commowick, Using bilateral symmetry to improve non-local means denoising of MR brain images, *International symposium on biomedical imaging (ISBI)*, San Francisco, USA, 2013, 1231-1234.
- [23] G. Chen, P. Zhang, Y. Wu, D. Shen, and P.-T. Yap, Collaborative non-local means denoising of magnetic resonance images, *IEEE 12th International symposium on biomedical imaging (ISBI)*, New York, USA, 2015, 564-567.
- [24] G. Chen, P. Zhang, Y. Wu, D. Shen, and P.-T. Yap, Denoising magnetic resonance images using collaborative non-local means, *Neurocomputing*, 2015, in press.
- [25] P. Coupé, P. Yger, S. Prima, P. Hellier, C. Kervrann, and C. Barillot, An optimized blockwise nonlocal means denoising filter for 3-D magnetic resonance images, *IEEE Transactions on Medical Imaging*, 27(4), 2008, 425-441.
- [26] J. Manjón, J. Carbonell-Caballero, J. Lull, G. García-Martí, L. Martí-Bonmatí, and M. Robles, MRI denoising using non-local means, *Medical Image Analysis*, 12(4), 2008, 514-523.
- [27] P. Zhang, M. Niethammer, D. Shen, and P.-T. Yap, Large deformation diffeomorphic registration of diffusion-weighted images with explicit orientation optimization, *Medical image computing and computer-assisted intervention (MICCAI)*, LNCS 8150, Nagoya, Japan, 2013.
- [28] P. Zhang, M. Niethammer, D. Shen, and P.-T. Yap, Large deformation diffeomorphic registration of diffusion-weighted imaging data, *Medical Image Analysis*, 18(8), 2014, 1290-1298.
- [29] P.-T. Yap, and D. Shen, Spatial transformation of DWI data using non-negative sparse representation, *IEEE transactions on medical imaging*, 31(11), 2012, 2035-2049.
- [30] S. F. Eskildsen and L. R. Østergaard, Quantitative comparison of two cortical surface extraction methods using MRI phantoms, *Medical image computing and computer-assisted intervention (MICCAI)*, LNCS 4791, Brisbane, Australia, 2007, 409-416.